

Toward a Maneuverable Miniature Robotic Fish Equipped With a Novel Magnetic Actuator System

Xingyu Chen, Junzhi Yu , Senior Member, IEEE, Zhengxing Wu, Yan Meng, and Shihan Kong

Abstract—Most existing robotic fish have a large body size driven by servo motor system, while conventional small-sized actuators hardly generate a high swimming performance. This paper reports a miniature untethered robotic fish, whose body length is 69 mm. In particular, a newly designed magnetic actuator system (MAS) is equipped, which guarantees both small-sized dimension and flexibility of the robot. More specifically, the magnetic field generated by a permanent magnet is first investigated based on Biot–Savart law. Then, a novel tail-beating rhythm called magnetically actuated pulse width modulation (MAPWM) is modeled for the new actuator system. Further, an MAPWM-based control method is presented, in which the duty ratio of MAPWM is innovatively utilized to realize the turning maneuvers for the first time. In addition, Lagrangian method is employed to establish the dynamic model to assess the MAPWM-based control method and the turning performance of the robotic fish. To further improve the maneuverability, the effect of a shape-variable caudal fin is analyzed based on computational fluid dynamics and the built dynamic model. Finally, combined with the MAS, the MAPWM-based control method, and the optimally selected caudal fin, extensive aquatic experiments are conducted on the robotic prototype. The results indicate that the developed miniature robotic fish achieves a considerably higher level of maneuverability in terms of turning radius when compared to swimming robots with equivalent dimensions.

Index Terms—Dynamic modeling, magnetic actuator system (MAS), maneuverability, robotic fish, underwater robot.

I. INTRODUCTION

GR^{EAT} progress has made in underwater intelligent systems, in which the role of underwater vehicle is becoming more prominent. Applications of underwater vehicles cover a variety of scenarios, such as underwater monitoring, search and rescue, data collection, exploration, and archaeology [1].

Manuscript received October 18, 2017; revised January 27, 2018; accepted March 1, 2018. This work was supported by the National Natural Science Foundation of China under Grant 61633020, Grant 61633017, Grant 61603388, Grant 61633004, and Grant 61725305. This paper was recommended by Associate Editor S. Nahavandi. (Corresponding author: Junzhi Yu.)

The authors are with the State Key Laboratory of Management and Control for Complex Systems, Institute of Automation, Chinese Academy of Sciences, Beijing 100190, China, and also with the University of Chinese Academy of Sciences, Beijing 100049, China (e-mail: chenxingyu2015@ia.ac.cn; junzhi.yu@ia.ac.cn; zhengxing.wu@ia.ac.cn; mengyan2017@ia.ac.cn; kongshihan2016@ia.ac.cn).

Color versions of one or more of the figures in this paper are available online at <http://ieeexplore.ieee.org>.

Digital Object Identifier 10.1109/TSMC.2018.2812903

As a bio-inspired underwater mobile platform, robotic fish has gradually received considerable attention due to some promising advantages, such as higher swimming efficiency, faster speed, enhanced maneuverability, and lower disturbance than traditional underwater vehicles propelled by screw-type thrusters [2]–[6]. In the past decades, many efforts have been devoted to developing robotic fish, which involves the studies of fish swimming propulsive mechanism, actuators, motion control, and so on. For example, Lauder and Tangorra [7] explored the theory of body and fin-based movements from the perspective of biology; Yu *et al.* [8] developed robotic fish to examine the control mechanism of central pattern generators; Butail *et al.* investigated the feasibility of regulating the collective behavior of zebrafish with a free-swimming robotic fish; and Wang *et al.* [28] investigated the path following control based on ribbon-fin propelled underwater vehicle.

Conventionally, middle- or large-sized robotic fish is developed, primarily because of sufficient space for mechatronic parts, battery package, and loads. Several studies have been reported on the small-sized robotic fish. For instance, Yu *et al.* [10] designed a miniature robotic fish to test multisensor system; Kopman *et al.* [11] developed a single-joint robotic fish for exploration of compliant tail; Bonnet *et al.* [12] utilized a miniature zebrafish lure for direct underwater interaction with living fish; and Abaid *et al.* [13] integrated a miniature robotic fish with the intelligent device for scientific education. It should be noted that a miniature robot usually has a dimension ranging from a few centimeters down to the millimeter scale [14]. Although the application of miniature robotic fish may not be qualified for a long-endurance mission, it can be envisaged as a tool for animal behavioral research and scientific education. Moreover, the miniature robotic fish can contribute to the hydromechanics research. Therefore, it is essential to investigate the miniature robotic fish.

No doubt the development of a miniature robotic fish is challenged by the actuator system in the context of mechanical drives. Although smart actuators are increasingly utilized to replicate fishlike swimming, they come with some drawbacks. Typically, Shuxiang *et al.* [15] made attempts to propel robotic fish with shape memory alloy and Heo *et al.* [16] addressed the design of a biomimetic fish robot actuated by piezoceramic. Yet, the effective vibration frequency or driving force of the two actuators is limited. Li *et al.* [17] constructed a robotic fish driven by a soft electroactive structure,

but it is driven by high voltage (over 7 kV). The expensive driving cost, as a result, will restrict its application. Marchese *et al.* [18] developed a robotic fish using fluidic elastomer, but the gas storage was complex and took up a significant amount of space. Though aforementioned advanced actuators have developed to some extent, servo motor system is still currently popular due to its good controllability and integration. It should not be neglected that the servo motor system brings relatively high power consumption and low energy conversion efficiency simultaneously, especially when to operate in reciprocated clockwise-and-anticlockwise rotation mode. Meanwhile, a servo motor-based system is not easy to be miniaturized in practice. By contrast, the magnetic actuator system (MAS) overcomes most drawbacks of aforementioned actuators effectively. For example, Tomie *et al.* [19] proposed a new turning method for magnetically driven fish-type microrobot and explored its turning performance based on magnetic field intensity and Takada *et al.* [20] also employed magnetic actuator in a photographing fish to produce rhythmic tail-beating. At present, the MAS yet has been struggling with some dilemmas on the vibration mode. The incompleteness of theoretical tail-beating model of MAS to some extent hinders the applicability of control methods in swimming control of robotic fish, which deserves to be fully explored.

Furthermore, the thrust of fishlike swimming in body/caudal fin mode largely comes from caudal fin, where different profiles or aspect ratios lead to different motion features. In the context of robotic implementation, Salumäe and Kruusmaa [21] explored the stiffness, profile, and geometry of caudal fin of real fish, and constructed an artificial caudal fin. Moreover, motion features produced by caudal fin are also affected by the adopted actuator. Thereby, it is necessary to jointly explore the features of caudal fin and its MAS to pursue better performance of the miniature robotic fish.

In this paper, a miniature single-joint zebrafish-like robotic fish (MIF-II) with a novel MAS is developed, whose total length is 69 mm. It is the updated version of MIF-I [22]. More specifically, for the purpose of enhanced maneuverability, a new MAS is presented to strike a balance between magnetic force and tail-beating amplitude. Benefiting from a well-designed rotatable adapting piece, the built MAS can efficiently realize the unique caudal oscillation. Meanwhile, the built MAS has a better capacity of harnessing the magnetic field. In order to investigate practical beating regularity, a novel tail-beating rhythm, named magnetically actuated pulse width modulation (MAPWM) is modeled, which deals with the caudal fins vibration as a uniformly accelerated motion. On this basis, an innovative control method is proposed for the robotic fish locomotion. For the first time, turning maneuvers can be easily achieved through adjusting the duty ratio of the MAPWM. As a well-integrated combination of the MAS, the MAPWM-based control method, and the optimally selected caudal fin, the developed MIF-II exhibits a substantially improved maneuverability, whose minimum length-specific turning radius is merely 0.29 body lengths (BLs). According to the authors' knowledge, this is the first time that maneuvering with a turning radius as low as

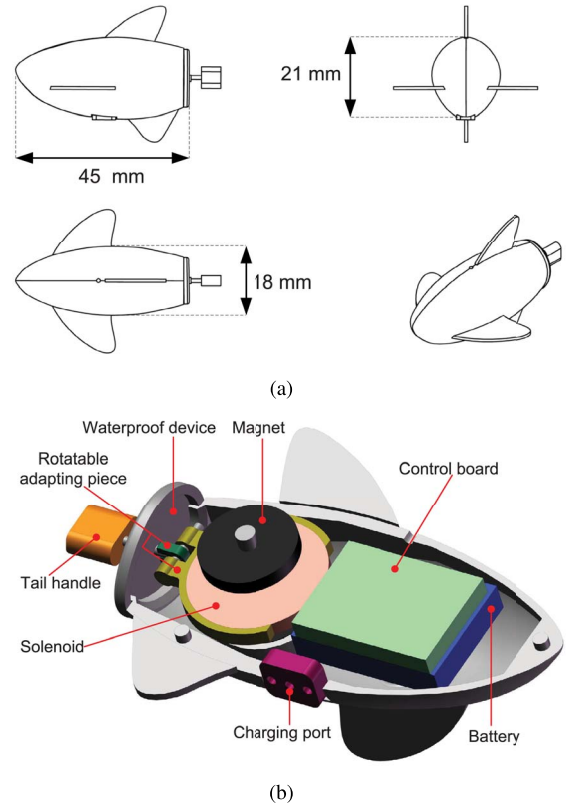


Fig. 1. Mechanical design of the conceived miniature robotic fish. (a) CAD drawing. (b) Mechanical structure.

0.29 BL has been successfully performed on a magnetically actuated miniature robotic fish.

The remainder of this paper is organized as follows. The overall mechatronic design of the miniature robotic fish equipped with the MAS is described in Section II. The magnetic model for the new actuator is established in Section III. Section IV analyzes the tail-related motion effect, and presents the MAPWM and the dynamics model simultaneously. The experimental results and analyses are provided in Section V. Finally, concluding remarks are offered in Section VI.

II. MECHATRONIC DESIGN OF THE ROBOTIC FISH WITH MAGNETIC ACTUATOR SYSTEM

In this section, the mechatronic design of the miniature robotic fish will be presented. Owing to several issues of servo motor system and other actuators mentioned in Section I, a carefully crafted MAS is built to generate vibration motion, which is characterized by small size and a tradeoff between the driving force and beating amplitude.

Fig. 1(a) shows the physical dimensions of the robotic fish. The fish body is 45 mm in length, 18 mm in width, and 21 mm in height. The layout of main components of the robotic fish is depicted in Fig. 1(b), in which two compartments, i.e., an electric compartment and an actuator compartment, can be divided. The electric compartment encompasses a control board, a mini Li-Po battery, and other facilitation designs.

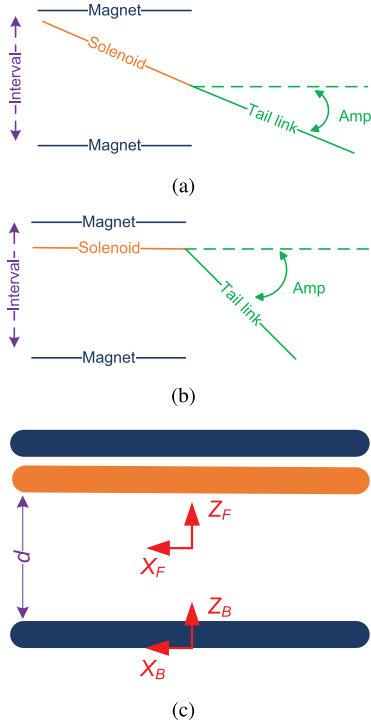


Fig. 2. Illustrative comparison of actuator in two generations of robotic fish. (a) Actuator in MIF-I. (b) Actuator in MIF-II. (c) Coordinate frame.

When it comes to the actuator compartment, a novel MAS is designed. The actuator system consists of a solenoid, two magnets, a peduncle, a rotatable adapting piece, and a flexible waterproof device. Functioning as an alternating field generator, the solenoid is in the control of direction-variable driven forces produced by two magnets. Most critically, a rotatable adapting piece is specially designed for altering the translation of the solenoid into the vibration of the tail. Though this modification requires a length-variable peduncle, the flexible connection mode can remedy the issue caused by a rigid one. On the part of the waterproof device, its role is threefold. The first function is to protect the internal electronics from water while the caudal fin is oscillating flexibly. Second, it works as a fulcrum. The third function is to facilitate the caudal fin to return to its initial position when the magnetic field is removed.

Concerning the problems with the deficient tail-beating amplitude and utilization rate of the magnetic field simultaneously, the MAS in MIF-II is a critically progressive version designed for MIF-I. Because of the rapid attenuation of magnetic flux density as distance increases, the two magnets are prohibited from a wide interval. As schematically shown in Fig. 2(a), the previous MAS does not work well in terms of the swing range. Moreover, the magnetic flux is wasted due to the rotation of solenoid verse magnets. On the contrary, as shown in Fig. 2(b), the updated MAS for MIF-II solves these two problems. The rotatable adapting piece converts the solenoid's translation into the vibration of the caudal fin, augmenting the amplitude to $\pi/6$, which obtains a huge improvement as opposed to the previous design for MIF-I ($\pi/12$). On the other

hand, by eliminating the vibration angle of the solenoid during the beating, the adapting piece guarantees the maximal utilization rate of the magnetic field at all times.

III. MAGNETIC MODEL FOR THE ACTUATOR SYSTEM

In this section, the model for magnetic flux density and force will be presented.

Based on Ampere's hypothesis of the electrodynamic molecule, the magnetic flux density produced by the magnet is treated as an impact brought by molecular circulation. Thus, Biot-Savart law [23] is employed to model the magnetic flux density

$$d\vec{B} = \frac{\mu_0}{4\pi} \frac{I d\vec{l} \times (\vec{r} - \vec{r}_0)}{|\vec{r} - \vec{r}_0|^3} \quad (1)$$

where $\mu_0 = 4\pi \times 10^{-7}$ denotes the vacuum permeability. $\vec{r} = [x, y, z]$ indicates a special point while the vector $r_0 = [x_0, y_0, z_0]$ stands for the position of magnetic source. I is the current, but for electrodynamic molecule in an axially magnetized object, $I = J_s dz_0$, where $J_s = \vec{M} \times \vec{n}$, and \vec{M} and \vec{n} stand for magnetization and externally normal vector, respectively. When $y > 0$, $d\vec{l} = [-dx_0, -dy_0, 0]$; otherwise $d\vec{l} = [dx_0, dy_0, 0]$.

With the aid of the frame $[X_B, Y_B, Z_B]$ defined in Fig. 2(c), the distribution of magnetic flux density produced by a magnet with radius R and thickness h can be formulated as follows:

$$\vec{B} = \int_0^h \frac{\mu_0 J_s dz_0}{4\pi} \oint_L \frac{d\vec{l} \times (\vec{r} - \vec{r}_0)}{|\vec{r} - \vec{r}_0|^3} = \int_0^h \frac{\mu_0 J_s dz_0}{4\pi} \times \left(\int_{-R}^R \frac{[-dx_0, \frac{x_0}{(R^2-x_0^2)^{1/2}} dx_0, 0]}{\left((x-x_0)^2 + (y-\sqrt{R^2-x_0^2})^2 + (z-z_0)^2\right)^{3/2}} \times [x-x_0, y-\sqrt{R^2-x_0^2}, z-z_0] \right. \\ \left. + \int_{-R}^R \frac{[dx_0, \frac{x_0}{(R^2-x_0^2)^{1/2}} dx_0, 0]}{\left((x-x_0)^2 + (y+\sqrt{R^2-x_0^2})^2 + (z-z_0)^2\right)^{3/2}} \times [x-x_0, y+\sqrt{R^2-x_0^2}, z-z_0] \right). \quad (2)$$

Splitting (2) in the cartesian frame, we have $B = B_x \vec{i} + B_y \vec{j} + B_z \vec{k}$

$$\left\{ \begin{aligned} B_x &= \frac{\mu_0 J_s}{4\pi} \int_0^h \int_{-R}^R \frac{(x_0(z-z_0))/(R^2-x_0^2)^{1/2}}{\left((x-x_0)^2 + (y-\sqrt{R^2-x_0^2})^2 + (z-z_0)^2\right)^{3/2}} \\ &\quad + \frac{(x_0(z-z_0))/(R^2-x_0^2)^{1/2}}{\left((x-x_0)^2 + (y+\sqrt{R^2-x_0^2})^2 + (z-z_0)^2\right)^{3/2}} dx_0 dz_0 \\ B_y &= \frac{\mu_0 J_s}{4\pi} \int_0^h \int_{-R}^R \frac{z-z_0}{\left((x-x_0)^2 + (y-\sqrt{R^2-x_0^2})^2 + (z-z_0)^2\right)^{3/2}} \\ &\quad + \frac{z_0-z}{\left((x-x_0)^2 + (y+\sqrt{R^2-x_0^2})^2 + (z-z_0)^2\right)^{3/2}} dx_0 dz_0 \\ B_z &= \frac{\mu_0 J_s}{4\pi} \int_0^h \int_{-R}^R \frac{(R^2-x_0^2)^{1/2} - y - (x_0(x-x_0))/(R^2-x_0^2)^{1/2}}{\left((x-x_0)^2 + (y-\sqrt{R^2-x_0^2})^2 + (z-z_0)^2\right)^{3/2}} \\ &\quad + \frac{(R^2-x_0^2)^{1/2} + y - (x_0(x-x_0))/(R^2-x_0^2)^{1/2}}{\left((x-x_0)^2 + (y+\sqrt{R^2-x_0^2})^2 + (z-z_0)^2\right)^{3/2}} dx_0 dz_0. \end{aligned} \right. \quad (3)$$

Thus, the magnetic flux intensity of the MAS can be numerically calculated. Fig. 3(a) and (b) shows the simulation results.

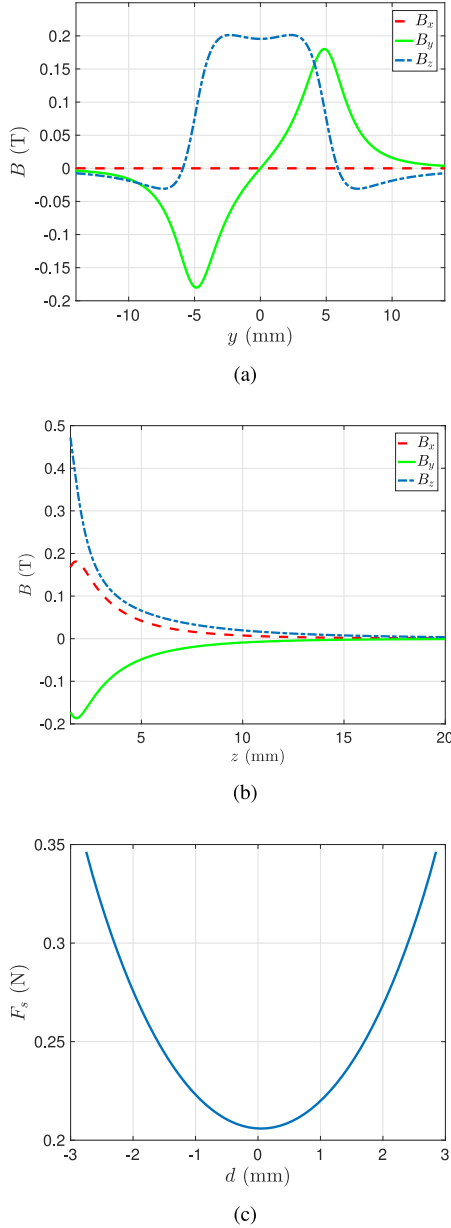


Fig. 3. Simulation results for magnetic flux intensity and force. (a) B versus y (or x) under the condition of x (or y) = 0 mm and $z = 3$ mm. (b) B versus z under the condition of $y = -3$ mm and $x = 3$ mm. (c) Resulting magnetic force.

Note that $J_s = 15$ is fixed to make the simulation more identical with the actual system. Other parameters involve $R = 5$ mm and $h = 1.5$ mm. Owing to only B_x and B_y contribute to the force on z -axis, it can be concluded that the area neighboring magnet edge can provide considerable magnetic flux intensity, which should be primarily utilized.

On the other hand, according to Ampere force, the magnetic force acting on a current loop \vec{F} can be calculated as follows:

$$d\vec{F} = I d\vec{l} \times \vec{B} \quad (4)$$

where I indicates the electric current in a solenoid, and \vec{B} denotes the magnetic flux density at some $d\vec{l}$. Similar to the analysis of B , the magnetic force F_c acting on a circular current

with radius r can be formulated as

$$F_c = I \int_{-r}^r \left\{ \left[dx_0, \frac{-x_0}{\sqrt{r^2 - x_0^2}}, 0 \right] \times \vec{B}(x_0, \sqrt{r^2 - x_0^2}, d) \right. \\ \left. + \left[-dx_0, \frac{-x_0}{\sqrt{r^2 - x_0^2}}, 0 \right] \times \vec{B}(x_0, -\sqrt{r^2 - x_0^2}, d) \right\}. \quad (5)$$

Assuming that a solenoid is composed of N layers while each layer contains n turns, and the wire diameter is d_w , the magnetic force F_s acting on the whole solenoid can then be formulated as

$$F_s = \sum_{j=1}^N \sum_{i=1}^n F_c(r(i), d(j)). \quad (6)$$

To further explore the variation of the driving force, as shown in Fig. 2(c), the above models are simulated in the frame $[X_F, Y_F, Z_F]$. The simulation parameters are set as $I = 0.3$ A, $R_s = 7$ mm, $H = 1.5$ mm, $d_w = 0.1$ mm, $n = R_s/d_w$, $N = H/d_w$, which are consistent with the actual system. As observed from Fig. 3(c), the distribution of the driving force in the 7-mm-wide interval is smoothly portrayed. The maximum 0.35 N occurs when the solenoid locates at the endpoints of the interval.

IV. MOTION ANALYSIS OF MAGNETICALLY ACTUATED ROBOTIC FISH

A. Caudal Fin-Based Fluid Coefficients

Considering that caudal fin has a great effect on the motion performance of a robotic fish, two main factors, i.e., fin profile and aspect ratio, will be optimized for enhanced maneuverability. Alternatively, as shown in Fig. 4(a), two typical profiles of the caudal fin are tested. In the meantime, the effect of aspect ratio σ is taken into account, which is calculated by $\sigma = L_c^2/S_2$, where L_c denotes the length of a caudal fin, and S_2 indicates its reference area, whose value is fixed at 430 mm² in this paper. In particular, three aspect ratios (i.e., 0.9, 1.3, and 2.1) are analyzed. In consideration of the coordination of fish's tail and body, these three aspect ratios represent the vertical distribution, the uniform distribution, and the horizontal distribution of the caudal fin in two-dimensional (2-D) space.

In the framework of hydrodynamics, different shapes correspond to different drag coefficients C^d and lift coefficients C^l which can be determined by using computational fluid dynamics (CFD) methods [24]. For an accurate and convenient CFD simulation, the commercial software ANSYS including ICEM CFD and Fluent can be employed. The simulation results on the effect of aspect ratio are shown in Fig. 4(b) and (c). This simulation clarifies the relation between fluid coefficients and angle of attack α , which is defined as the angle between the tangent of the caudal fins's path and the axis of the fins chord [30]. At the same angle of attack α , higher aspect ratio means higher lift coefficient and faster drag augment. Meanwhile, a large aspect ratio causes C^l of profile A change more acutely while the small one has little effect on it.

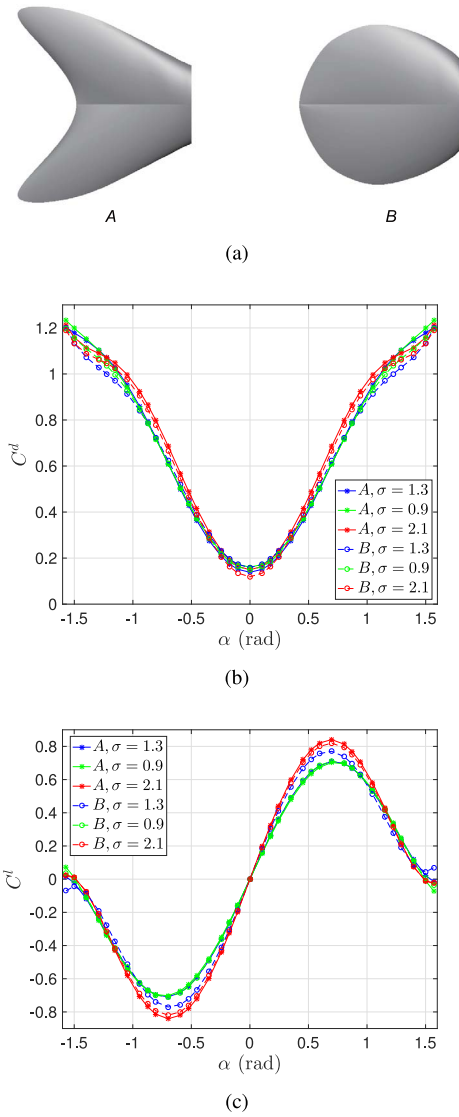


Fig. 4. Selection of caudal fin. (a) Two typical profiles of caudal fin. (b) Simulated drag coefficients versus attack angle. (c) Simulated lift coefficients versus attack angle.

Relatively, the effect of aspect ratio on C^l of profile B is more well-proportioned.

B. Magnetically Actuated Pulse Width Modulation Method

Because of different operating characteristics of actuators, the tail-beating rhythm generated by the MAS differs from that produced by servo motor system, meaning a nonsinusoidal vibration. According to the analysis in Section III, the vibration generated by the MAS is not smooth in the air, and the case is more complex underwater. Since the fluid resistance may balance the rise or fall of magnetic force instantaneously, as analyzed in the previous sections, the variation range of the solenoid translation or the magnetic force is narrow. For simplicity, it is assumed that the tail-beating is a uniformly accelerated vibration. Hence, the resistance or angular acceleration can be estimated as follows.

It is not difficult to fit the simulation result in Fig. 3(c) with a polynomial

$$F_s = 0.1e^{-395.7d} + 0.1e^{395.7d}. \quad (7)$$

When the caudal fin vibrates underwater but the robotic fish maintains still, it would experience magnetic force F_s and drag force F_D , the latter of which can be calculated as [25]

$$F_D = -\text{sgn}(\omega) \frac{1}{2} \rho C_p^d S_2 (\omega L_t)^2 \quad (8)$$

where ρ denotes the density of the water, having $\rho = 10^3 \text{ kg/m}^3$. C_p^d indicates the perpendicular drag coefficient, approximately having $C_p^d = 1.1$, which is obtained by the simulation in Section IV-A.

Thus, the angular acceleration can be obtained as

$$a_w(k) = (F_s L_s + F_D L_t) / I_t \quad (9)$$

where the force arms $L_s = L_t = 5 \text{ mm}$, and $I_t = 1.25 \times 10^{-6} \text{ kgm}^2$ is the moment of inertia of the caudal fin.

Moving one step further, we can obtain a group of iteration

$$\begin{cases} d(i) = L_s \tan(\phi(i)) \\ F_s(i) = 0.1e^{-395.7d(i)} + 0.1e^{395.7d(i)} \\ F_D(i) = -\text{sgn}(\omega(i)) \frac{1}{2} \rho C_p^d S_2 (\omega(i) L_t)^2 \\ a_w(i) = (F_s(i) L_s + (F_D(i) + F_e(i)) L_t) / I_t \\ \omega(i+1) = \omega(i) + a_w(i) dt \\ \phi(i+1) = \phi(i) + \omega(i) dt. \end{cases} \quad (10)$$

Thus, as depicted in Fig. 5(a), the variation of ω during a complete swing can be simulated. Though its growth is hard to precisely describe, ω can be fitted linearly, and the slope 975.3 rad/s^2 can be treated as the angular acceleration a_w . Furthermore, the tail-beating rhythm termed MAPWM can be constructed, as shown in Fig. 5(b). In essence, it is a cycle signal with the frequency f . Define the duty ratio D as the ratio between the time of $\phi > 0$ and the period. Then, the motion parameters f and D are of crucial importance in the MAPWM-based control method. It is worthwhile to note that D is analogous to the bias in the servo motor system. That is, when it is not equal to 0.5, imbalance of vibration will occur, leading to turning motions.

C. Motion Model for the Robotic Fish

In order to predict the turning performance, a dynamic model of fishlike swimming is established based on the Lagrange approach [26]. For the sake of simplicity, it is assumed that the robotic fish can be formulated as a two-rigid-body system; the robotic fish swims in still water; and the impact from ripple is ignored.

To clearly describe the fishlike swimming dynamics, coordinate systems are illustrated in Fig. 6, including a global inertial reference frame denoted by $O - X_w Y_w Z_w$, and two body-fixed moving reference frames denoted by $O_b - X_b Y_b Z_b$ and $O_t - X_t Y_t Z_t$, respectively. According to the above assumptions, the fish body and caudal fin have been separately simplified as two links. Since only the planar swimming is considered, let $\{X, Z, \Theta\}$ be the status of the mass center of the robot. Meanwhile, let $r_i = (X_i^f, 0, Z_i^f)^T$ be the centroid of two links

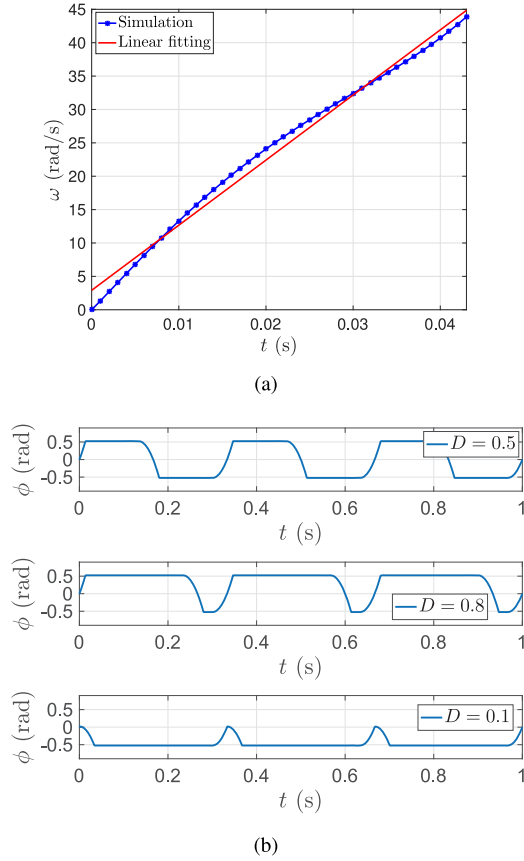


Fig. 5. Illustration of MAPWM method. (a) History of the simulated ω and its linear fitting. (b) Plot of MAPWM, where the frequency is 3 Hz while the duty ratio equals to 0.5, 0.8, and 0.1.

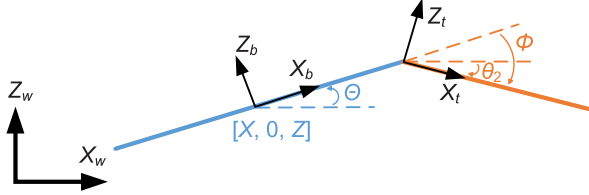


Fig. 6. Schematic of a two-link model and its coordinate frames.

and l_i^f be a relevant link length, both expressed in $O - XYZ$. Thus, we have

$$\begin{cases} r_1 = [X, 0, Z]^T \\ r_2 = r_1 + R_b^w [l_1^f, 0, 0]^T + R_t^w [l_2^f, 0, 0]^T \end{cases} \quad (11)$$

where R_b^w and R_t^w denote the transformation matrices from the body reference frames to the global one, which have the following expressions:

$$\begin{cases} R_b^w = \begin{bmatrix} \cos \Theta & 0 & -\sin \Theta \\ 0 & 1 & 0 \\ \sin \Theta & 0 & \cos \Theta \end{bmatrix} \\ R_t^w = \begin{bmatrix} \cos \theta_2 & 0 & -\sin \theta_2 \\ 0 & 1 & 0 \\ \sin \theta_2 & 0 & \cos \theta_2 \end{bmatrix} \end{cases} \quad (12)$$

where θ_2 can be obtained through Θ and the joint angle ϕ as follows:

$$\theta_2 = \Theta + \phi. \quad (13)$$

Next, the translative velocities v_i and angular velocities ω_i of the center of mass of the i th link with respect to the global reference frame $O - XYZ$ can be obtained as

$$\begin{cases} v_i = \dot{r}_i \\ \omega_i = \dot{\Theta}_i. \end{cases} \quad (14)$$

Therefore, the Lagrangian equation can be written as the sum of potential energy denoted by E and kinetic energy which contains both the translational and the rotational kinetic energy of the miniature robotic fish

$$L = \sum_{i=1}^2 \frac{1}{2} m_i v_i^2 + \sum_{i=1}^2 \frac{1}{2} I_i \omega_i^2 + E \quad (15)$$

where m_i and I_i represent the mass and angular inertia of each link, including the added mass and inertia.

The Lagrangian equations of the second kind can then be given by

$$\begin{cases} F_X = \frac{d}{dt} \frac{\partial L}{\partial \dot{X}} - \frac{\partial L}{\partial X} \\ F_Z = \frac{d}{dt} \frac{\partial L}{\partial \dot{Z}} - \frac{\partial L}{\partial Z} \\ M_\Theta = \frac{d}{dt} \frac{\partial L}{\partial \dot{\Theta}} - \frac{\partial L}{\partial \Theta}. \end{cases} \quad (16)$$

The hydrodynamic forces acting on the robotic fish are decided by the instantaneous movement. Here, a hydrodynamic drag model is leveraged to analyze the forces perpendicular to the surface of the head link, which has been adopted in the case of large Reynolds number [26], while the lift force model is still utilized for the tail link analysis. Before numerical estimation, we need first obtain the velocities expressed in the body-fixed reference frames

$$\begin{cases} v_1^b = (R_b^w)^T v_1 \\ v_2^b = (R_t^w)^T v_2. \end{cases} \quad (17)$$

Thus, the hydrodynamic force on head link could be divided into pressure (F_1^p) and drag (F_1^d) while the lift (F_2^l) and drag (F_2^d) act on the tail link, which can be calculated by

$$\begin{cases} F_1^p = -\frac{1}{2} \rho C_1^p S_1^p |v_1^b(3)| v_1^b(3) \\ F_1^d = -\frac{1}{2} \rho C_1^d S_1^d |v_1^b(1)| v_1^b(1) \\ F_1 = [F_1^d, 0, F_1^p]^T. \end{cases} \quad (18)$$

Meanwhile, the lift force and drag on the tail link can be given as

$$\begin{cases} F_2^l = \frac{1}{2} \rho C_2^l S_2 |v_2^l|^2 \\ F_2^d = \frac{1}{2} \rho C_2^d S_2 |v_2^l|^2 \\ F_1 = [F_2^d \cos \alpha - F_2^l \sin \alpha, 0, F_2^d \sin \alpha + F_2^l \cos \alpha]^T \end{cases} \quad (19)$$

where the coefficients C^p , C^l , and C^d represent pressure coefficient, lift coefficient, and drag coefficient, which can be obtained through the simulation in Section IV-A; ρ denotes the water density; and $S_1^d = 285 \text{ mm}^2$, $S_1^p = 891 \text{ mm}^2$, and $S_2 = 430 \text{ mm}^2$ are wetted areas.

Then, the hydrodynamic forces need transform into the global inertial reference frame

$$\begin{cases} F_1^w = R_b^w F_1 \\ F_2^w = R_t^w F_2 \\ M^w = (r_1 - r_0) \times F_2^w. \end{cases} \quad (20)$$

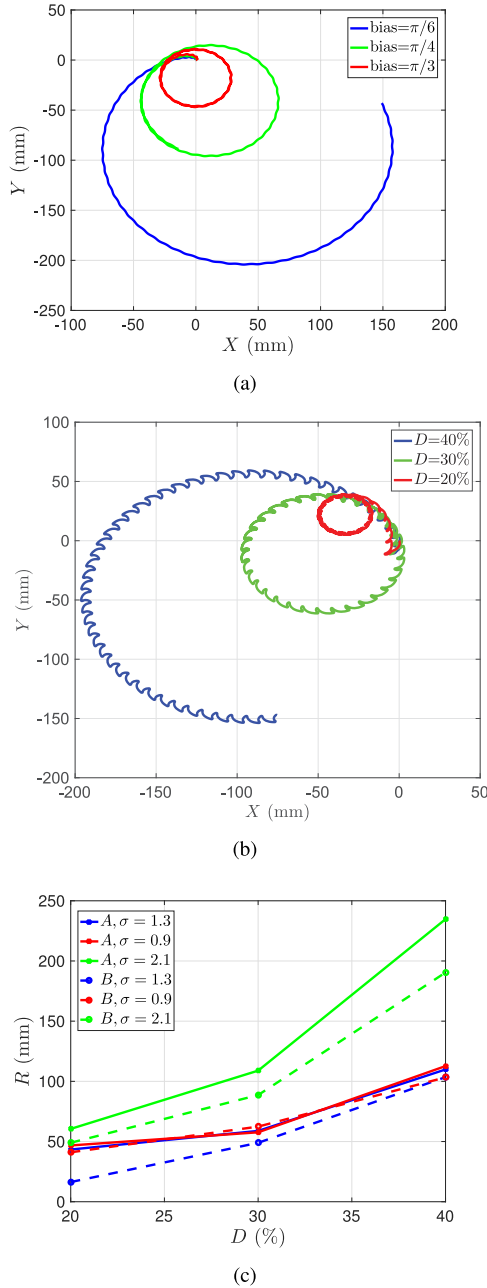


Fig. 7. Comparison of two motion modes. (a) Simulated trajectory with the sinusoidal tail-beating motion mode. (b) Simulated trajectory with the MAPWM tail-beating motion mode. (c) Simulated turning radius versus the duty ratio of the MAPWM.

Based on the above analyses, we can get the generalized forces and moments expressed in the global inertial frame as follows:

$$\begin{cases} F_X = F_1^w(1) + F_2^w(1) \\ F_Z = F_1^w(3) + F_2^w(3) \\ M_\Theta = M^w. \end{cases} \quad (21)$$

Eventually, the turning performance of the miniature robotic fish can be estimated with the above-derived equations. Fig. 7 demonstrates a comparative simulation lasting 10 s, where the working frequency is set as 5 Hz. More specifically, sinusoidal tail-beating motion mode and MAPWM-tail-beating motion

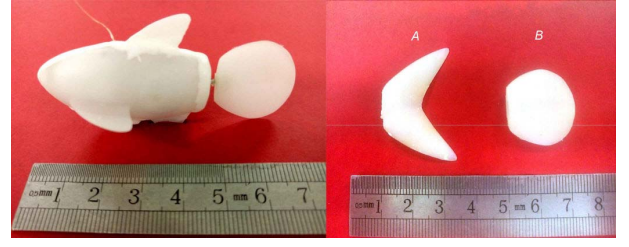


Fig. 8. Photograph of the tested robotic prototype and the caudal fins.

mode are compared. Once the robotic fish starts moving, bias is superposed to initiate turning motions in the former mode, while the MAPWM-based control method is employed to modulate duty ratio so as to generate turning motions in the latter mode. As seen from Fig. 7(a) and (b), smaller turning-radius is achieved in the MAPWM-based control method, whereas smoother moving trajectory is obtained in the sinusoidal tail-beating motion mode. In reality, the role of the variable duty ratio in the MAPWM-based motion system is similar to the bias in the sinusoidal motion system.

In addition, according to our preliminary test results [22], the robotic fish possibly achieves the highest maneuverability when the frequency ranges from 4.4 to 5.9 Hz while the duty ratio is limited between 15% to 27% (or, 73% to 85%). Thus, another comparison for shape-variable caudal fin is conducted with the parameters of $f = 5$ Hz and $D = 20\% - 40\%$. Combined with the different fluid coefficients simulated in Section IV-A, a group of the turning radius R can be obtained. As shown in Fig. 7(c), the tail with profile *B* exhibits the highest maneuverability, whose aspect ratio equals 1.3. After careful scrutiny of simulation data, it is found that excessively high aspect ratio is not suitable for a flexible MAS. It is noteworthy that a large attack angle (e.g., $\alpha > 60^\circ$) often occurs in the MIPWM-control system during turning. In such a circumstance, C^l of all the caudal fins decreases while the C^d of the optimally selected tail works better.

V. EXPERIMENTS AND ANALYSES

A. Experimental Setup and Model Validation

In this section, extensive aquatic experiments were carried out based on MAPWM-based control method. We focused on the 2-D turning performances generated by the MAS and the two typical tails analyzed in Section IV. The aquatic experiments were executed in a 4-m-long and 5-m-wide tank with a camera installed 1.9 m above the water surface for video data collection. Through vision measurement, the data of turning radius and angular speed can be acquired, which reveal the turning performance of the robotic fish.

According to the simulation in Section IV, the caudal fin with profile *B* was selected for experiments, with an aspect ratio of 1.3. Alternatively, the caudal fin with profile *A* and $\sigma = 0.9$ was utilized as a comparison. For the convenience of description, the aforementioned two caudal fins are denoted by *B* and *A*, respectively. Fig. 8 presents the robotic prototype and the caudal fins in this experiments.

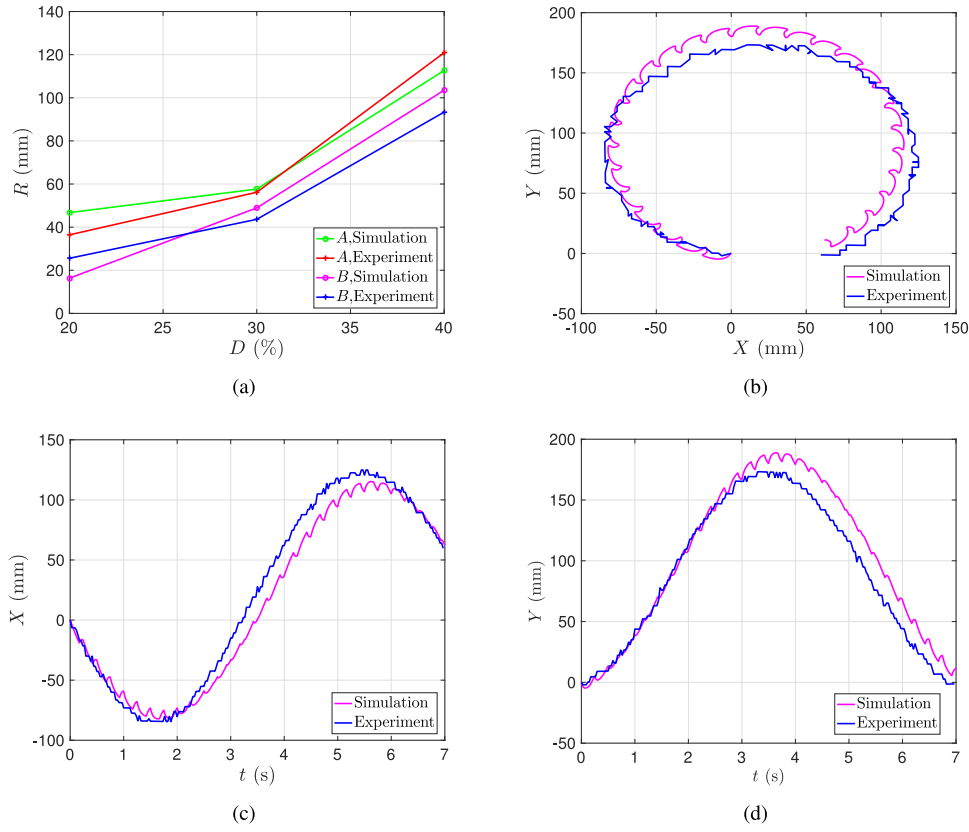


Fig. 9. Comparative results on turning performance test. (a) Turning radius. (b)–(d) Rotational trajectory comparison.

The validity of the proposed dynamic model was verified at first. As illustrated in Fig. 9, the experimental data and simulation data were compared. Fig. 9(a) shows the comparison of turning radius for A and B at the frequency of 5 Hz. These two groups of data show the same trend approximately. Fig. 9(b)–(d) shows rotational trajectories generated by simulation and experiment with the parameters of $f = 4$ Hz and $D = 30\%$. These comparisons show a good agreement between the simulated and experimental data, confirming the effectiveness of dynamic modeling.

B. Straight Line Swimming

When $D = 50\%$, the robotic fish swim along a straight line approximately. We alter the tail-beating frequency from 2 to 7 Hz to investigate the swimming speed V . As a result, $V = 60.5, 79.1, 83.2, 85.2, 78.0, 69.4$ mm/s, respectively. It is obvious that the straight speed first increases and then decreases as the tail-beating frequency raising. The peak locates at the frequency of 5 Hz, whose value is 85.2 mm/s or 1.23 BL/s. However, the speed decreases when the frequency is quite high. This phenomenon is brought by mechanical response speed. That is, a period is not enough for a full vibration if the frequency is too high.

C. Rotational Maneuvers

To explore the maneuverability of the robotic fish, more comprehensive experiments were conducted. Unlike the

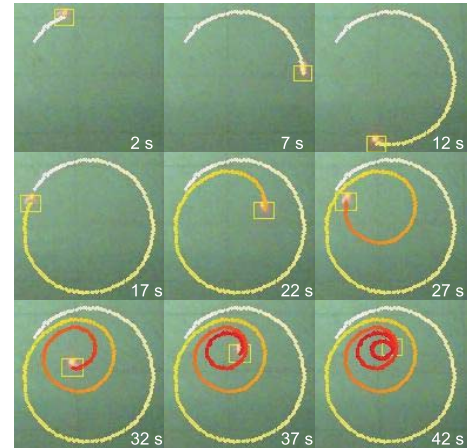


Fig. 10. Snapshot sequence of circular motion. Note that the moving trajectory is plotted using KCF tracking algorithm.

motor-driven robotic fish, the turning motions of the robotic fish with the MAS mainly depend on the tail-beating frequency and the duty ratio of MAPWM. As shown in Fig. 10, the miniature robotic fish swam as an expected helical trajectory, revealing a high maneuverability of the robotic fish. This maneuver was conducted with the parameters of $f = 4$ Hz and $D = 40\% - 10\%$. Furthermore, the frequency was varied from 2 Hz to 7 Hz while the duty ratio was altered from 40% to 10%. As shown in Fig. 11, massive experimental data were obtained and analyzed. Fig. 11(a) and (b) illustrates the data of

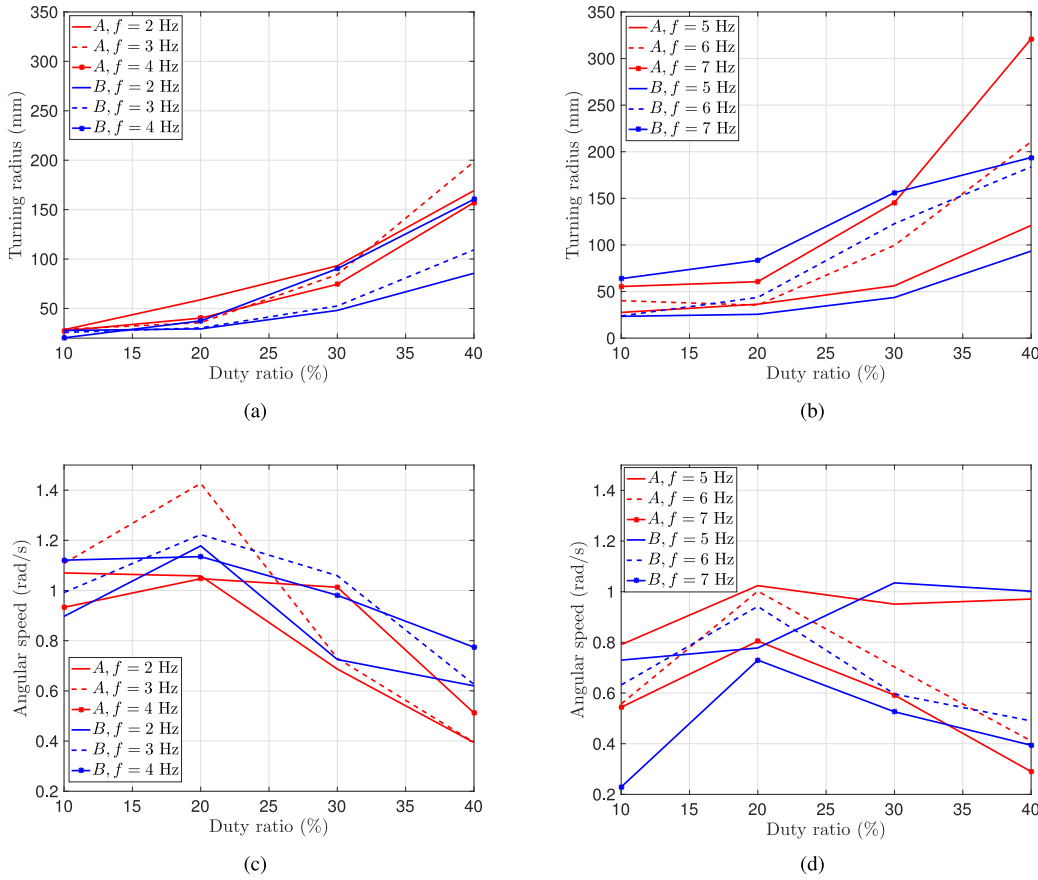


Fig. 11. Experimental results of turning radius and average angular speed. (a) Low-frequency turning radius versus duty ratio. (b) High-frequency turning radius versus duty ratio. (c) Low-frequency angular speed versus duty ratio. (d) High-frequency angular speed versus duty ratio.

turning radius under the condition of a fixed tail-beating frequency, which indicates that there is a wide range of radius. The minimum is 20.28 mm, which is length-specifically equivalent to 0.29 BL, corresponding to the motion parameters of $f = 4$ Hz and $D = 10\%$. Hence, thanks to the novel mechanism of the MAS and optimally selected shape of the caudal fin, there is a great improvement for the maneuverability, compared with MIF-I, whose minimum turning radius is 183.14 mm or 2.05 BL. Fig. 11(c) and (d) illustrates the variation of average angular speed in this experiments. The maximal one is 1.22 rad/s for the caudal fin *B*. In terms of the attained turning radius and average angular speed, the miniature robotic fish achieves a high maneuverability with the MAPWM-based control method.

Some conclusions can further be drawn based on the comparison between the experimental data measured with *A* and *B*. In terms of radius data, the minimum turning radius is 20.28 mm for *B* while 27.44 mm for *A*, which are both obtained by the parameters of $f = 4$ Hz and $D = 10\%$. It implies that most maneuverability related parameters are determined by the MAS. The caudal fin, indeed, affects the turning performance. The advantage of *B* is more evident as the frequency keeps 4 Hz away. Specifically, the turning radii are more distinct at the frequency of 2 and 3 Hz. The main reason is the feature of MAPWM-tail-beating motion mode. That is, the caudal swing can be treated as a uniformly accelerated

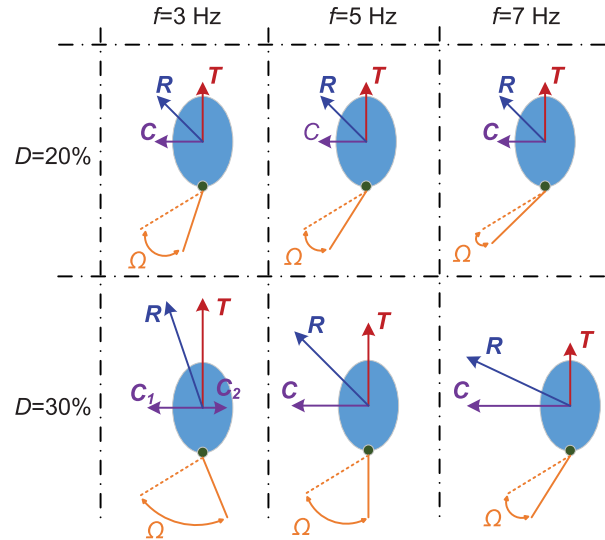


Fig. 12. Diagram of the turning process and force condition. The blue patch is the fish body while the orange line represents the tail. Besides, Ω denotes the swing range. The resultant force R is synthesized by the thrust T and centripetal force C .

vibration, and the angular acceleration is related to the magnetic field rather than tail-beating frequency. Thus, the swing time ratio in a period would become small, if tail-beating frequency becomes lower. When tail keeps still at the amplitude,

TABLE I
MINIMUM TURNING RADIUS COMPARISON WITH EXISTING WORK

Literature	Body length	Minimum turning radius
Phamduy <i>et al.</i> [27]	66 mm	1.0 BL (66 mm)
Tomie <i>et al.</i> [19]	64 mm	0.55 BL (35 mm)
Chen <i>et al.</i> [22]	89 mm	2.05 BL (183 mm)
This paper	69 mm	0.29 BL (20 mm)

the turning motion is not affected by the fluid coefficients, and the inertia would amplify minor effect brought by the caudal fin. In terms of angular speed, it first increases and then decreases as D increasing in many cases. However, this trend does not appear at $f = 5$ Hz. Many factors cause this exception, but the main reason is the condition of thrust and centripetal force. We illustrate Fig. 12 to compare the force conditions when $D = 20\% - 30\%$, in which Ω decided by the MAS represents the swing range of caudal fin in a particular condition. The miniature robotic fish turns under the influence of thrust and centripetal force, and both the magnitude and direction of their resultant force affect turning motion. If the swing range closes to the central axis of the body, the tail beating contributes more to thrust. Otherwise, centripetal force benefits more from caudal vibration. Therefore, although Ω increases with the rise of D , there are different effects on turning performance for different tail-beating frequency. In particular, as shown in Fig. 12, the direction of the resultant force is always in favor of turning at $f = 5$ Hz. On the contrary, when $D = 30\%$, the resultant force promotes forward swimming if $f < 5$ Hz whereas it does harm to motion if $f > 5$ Hz. Consequently, in terms of the turning radius and average angular speed, the miniature robotic fish performs the most flexible turning motion at the frequency of 5 Hz. Furthermore, Table I compares some magnetically actuated miniature robotic fishes with this paper in terms of minimum turning radius. As can be observed, the developed miniature robotic fish achieves the minimum turning radius of 0.29 BL, representing a big step forward in implementing turns in tight spaces. Accidentally, to the best of our knowledge, it may be the minimum turning radius achieved by the miniature robotic fish at the moment.

D. Discussion

High maneuverability is a critical survival skill for natural fish. Likewise, it is worthwhile to replicate this feature on the bio-inspired underwater robots to meet the ever-increasing demands of ocean exploitation and military operations. The maneuverability for middle- or large-sized robotic fish has been extensively investigated. For example, based on a pair of undulating pectoral fins, Wei *et al.* [29] developed robotic cuttlefish to achieve zero-radius turning performance. However, the maneuverability issue of the miniature robotic fish is rarely tackled. One of the main reasons is for the lack of small-sized and powerful actuator system. Traditional miniature MAS has a major drawback, i.e., the tradeoff between driving force and beating amplitude. Phamduy *et al.* [27] developed their device using an annular solenoid, whose outer diameter was 10 mm and inner diameter was 7 mm. Meanwhile, two $\Phi 4.7 \times 1.6$ -mm-size magnets were adopted in their system, and

the beating amplitude was around $\pi/12$ rad. Tomie *et al.* [19] designed an MAS depending on controllable magnetic field strength and a rotatable magnet. The amplitude can reach $\pi/5$ rad when the magnetic field strength is raised to 800 A/m, whereas the amplitude decreases quickly to $\pi/12$ rad at low frequencies below 5 Hz. The MAS in MIF-I was composed of two $\Phi 10 \times 3$ -mm-size magnets and a $\Phi 10 \times 3$ -mm-size solenoid, and the beating amplitude generated was limited to $\pi/12$ rad as well. For the MAS in MIF-II, it involves two $\Phi 10 \times 1.5$ -mm-size magnets and a $\Phi 14 \times 1.5$ -mm-size solenoid, which is seemingly not as powerful as that in MIF-I. Contributed by the rotatable adopting piece, the new MAS, on the contrary, reaches a beating amplitude of $\pi/6$ while maintaining the sufficient magnetic force. Crucially, the rotatable adopting piece is created to remedy the aforementioned problems, whose function is twofold: 1) elimination of the rotation of the solenoid verse magnets, which contributes to the increased utilization rate of the magnetic field and 2) shortening the length of driving arm of caudal lever, which is beneficial to augment of the beating amplitude. Of course, this improvement comes with certain side effects. In particular, the shorter driving arm demands a stronger driving force, and the peduncle has to be stretched out and drew back repeatedly during the vibration. Thanks to the careful design, the improvement plays a leading role.

VI. CONCLUSION

In this paper, we have developed a maneuverable miniature robotic fish equipped with a novel MAS, in which a particular rotatable adopting piece is designed for enhancing the turning maneuvers of the robot. Thanks to the alternating field, the miniature fish is able to perform untethered fishlike swimming. Based on Biot–Savart law, we analyze the magnetic force in the fish body. Then, we build a new tail-beating rhythm, namely MAPWM. Distinct from the traditional sinusoidal vibration, the MAPWM is more close to the practical beating regularity, which is treated as a uniformly accelerated vibration. Accordingly, an MAPWM-based control method is proposed, which creatively makes use of the duty ratio to govern the turning motion of the robotic fish. Furthermore, the dynamic model is established based on Lagrange method, contributing to explore the MAPWM-based control method and the maneuverability of the robotic fish. On the other hand, through fluid simulation, we optimally select the shape of caudal fin for better turning performance. Finally, we conduct extensive experiments based on the MAPWM-based control method. The comparative results further show that the constructed miniature robotic fish attains a considerably higher level of maneuverability than the existing swimming robots with equivalent dimensions, offers a promising perspective for design and control of the MAS applied to fishlike swimming robots.

In the near future, some advanced control algorithms will be planned for real-world tasks, and some sensors will be incorporated for better intelligence and interaction ability. In addition, the better control algorithm and bigger-size magnetic actuator will be investigated.

REFERENCES

- [1] D. Shin, S. Y. Na, J. Y. Kim, and S.-J. Baek, "Fish robots for water pollution monitoring using ubiquitous sensor networks with sonar localization," in *Proc. Int. Conf. Conver. Inf. Technol.*, Gyeongju, South Korea, Nov. 2007, pp. 1298–1303.
- [2] L. Wen, T. Wang, G. Wu, and J. Liang, "Quantitative thrust efficiency of a self-propulsive robotic fish: Experimental method and hydrodynamic investigation," *IEEE/ASME Trans. Mechatronics*, vol. 18, no. 3, pp. 1027–1038, Jun. 2013.
- [3] J. Yu, Z. Su, Z. Wu, and M. Tan, "An integrative control method for bio-inspired dolphin leaping: Design and experiments," *IEEE Trans. Ind. Electron.*, vol. 63, no. 5, pp. 3108–3116, May 2016.
- [4] J. Conte, Y. Modarres-Sadeghi, M. N. Watts, F. S. Hover, and M. S. Triantafyllou, "A fast-starting mechanical fish that accelerates at 40 ms^{-2} ," *Bioinspiration Biomimetics*, vol. 5, no. 3, 2010, Art. no. 035004.
- [5] J. Yuan, Z. Wu, J. Yu, and M. Tan, "Sliding mode observer-based heading control for a gliding robotic dolphin," *IEEE Trans. Ind. Electron.*, vol. 64, no. 8, pp. 6815–6824, Aug. 2017.
- [6] J. Yu, L. Wen, and Z. Ren, "A survey on fabrication, control, and hydrodynamic function of biomimetic robotic fish," *Sci. China Technol. Sci.*, vol. 60, no. 9, pp. 1365–1380, 2017.
- [7] G. V. Lauder and J. L. Tangorra, "Fish locomotion: Biology and robotics of body and fin-based movements," in *Robot Fish*, R. Du, Z. Li, K. Youcef-Toumi, and P. Valdivia y Alvarado, Eds. Heidelberg, Germany: Springer, 2015, pp. 25–49.
- [8] J. Yu, M. Wang, W. Wang, M. Tan, and J. Zhang, "Design and control of a fish-inspired multimodal swimming robot," in *Proc. IEEE Int. Conf. Robot. Autom.*, Shanghai, China, May 2011, pp. 3664–3669.
- [9] S. Butail, T. Bartolini, and M. Porfiri, "Collective response of zebrafish shoals to a free-swimming robotic fish," *PLoS ONE*, vol. 8, no. 10, 2013, Art. no. e76123.
- [10] J. Yu, S. Chen, Z. Wu, and W. Wang, "On a miniature free-swimming robotic fish with multiple sensors," *Int. J. Adv. Robot. Syst.*, vol. 13, no. 2, pp. 1–8, 2016.
- [11] V. Kopman, J. Laut, F. Acquaviva, A. Rizzo, and M. Porfiri, "Dynamic modeling of a robotic fish propelled by a compliant tail," *IEEE J. Ocean. Eng.*, vol. 40, no. 1, pp. 209–221, Jan. 2015.
- [12] F. Bonnet, Y. Kato, J. Halloy, and F. Mondada, "Infiltrating the zebrafish swarm: Design, implementation and experimental tests of a miniature robotic fish lure for fish-robot interaction studies," *Artif. Life Robot.*, vol. 21, no. 3, pp. 239–246, 2016.
- [13] N. Abaid *et al.*, "Controlling a robotic fish with a smart phone," *Mechatronics*, vol. 23, no. 5, pp. 491–496, 2013.
- [14] P. Valdastrì *et al.*, "A novel magnetic actuation system for miniature swimming robots," *IEEE Trans. Robot.*, vol. 27, no. 4, pp. 769–779, Aug. 2011.
- [15] G. Shuxiang, T. Fukuda, and K. Asaka, "A new type of fish-like underwater microrobot," *IEEE/ASME Trans. Mechatronics*, vol. 8, no. 1, pp. 136–141, Mar. 2003.
- [16] S. Heo, T. Wiguna, H. C. Park, and N. S. Goo, "Effect of an artificial caudal fin on the performance of a biomimetic fish robot propelled by piezoelectric actuators," *J. Bionic Eng.*, vol. 4, no. 3, pp. 151–158, 2007.
- [17] T. Li *et al.*, "Fast-moving soft electronic fish," *Sci. Adv.*, vol. 3, no. 4, 2017, Art. no. e1602045.
- [18] A. D. Marchese, C. D. Onal, and D. Rus, "Autonomous soft robotic fish capable of escape maneuvers using fluidic elastomer actuators," *Soft Robot.*, vol. 1, no. 1, pp. 75–87, 2014.
- [19] M. Tomie, A. Takiguchi, T. Honda, and J. Yamasaki, "Turning performance of fish-type microrobot driven by external magnetic field," *IEEE Trans. Magn.*, vol. 41, no. 10, pp. 4015–4017, Oct. 2005.
- [20] Y. Takada, K. Koyama, and T. Usami, "Position estimation of small robotic fish based on camera information and gyro sensors," *Robotics*, vol. 3, no. 2, pp. 149–162, 2014.
- [21] T. Salumäe and M. Kruusmaa, "A flexible fin with bio-inspired stiffness profile and geometry," *J. Bionic Eng.*, vol. 8, no. 4, pp. 418–428, 2011.
- [22] X. Chen, Z. Wu, Z. Chao, and J. Yu, "Design and implementation of a magnetically actuated miniature robotic fish," in *Proc. 20th World Congr. Int. Federation Autom. Control*, Toulouse, France, Jul. 2017, pp. 7045–7050.
- [23] R. C. Haddon, "The application of the Biot–Savart law to the ring current analysis of proton chemical shifts—II: An approach to aromatic character in the annulenes," *Tetrahedron*, vol. 28, no. 14, pp. 3635–3655, 1972.
- [24] Z. Wu, J. Yu, J. Yuan, M. Tan, and J. Zhang, "Mechatronic design and implementation of a novel gliding robotic dolphin," in *Proc. IEEE Int. Conf. Robot. Biomim.*, Zhuhai, China, Dec. 2015, pp. 267–272.
- [25] K. A. Morgansen, B. I. Triplett, and D. J. Klein, "Geometric methods for modeling and control of free-swimming fin-actuated underwater vehicles," *IEEE Trans. Robot.*, vol. 23, no. 6, pp. 1184–1199, Dec. 2007.
- [26] C. Zhou, Z.-G. Hou, Z. Cao, S. Wang, and M. Tan, "Motion modeling and neural networks based yaw control of a biomimetic robotic fish," *Inf. Sci.*, vol. 237, pp. 39–48, Jul. 2013.
- [27] P. Phamduy *et al.*, "Design and characterization of a miniature free-swimming robotic fish based on multi-material 3D printing," *Int. J. Intell. Robot. Appl.*, vol. 1, no. 2, pp. 209–223, 2017.
- [28] R. Wang, S. Wang, Y. Wang, M. Tan, and J. Yu, "A paradigm for path following control of a ribbon-fin propelled biomimetic underwater vehicle," *IEEE Trans. Syst., Man, Cybern., Syst.*, to be published, doi: 10.1109/TSMC.2017.2705340.
- [29] Q. Wei, S. Wang, C. Zhou, and M. Tan, "Course and depth control for a biomimetic underwater vehicle—RobCutt-I," *Int. J. Offshore Polar Eng.*, vol. 25, no. 2, pp. 81–87, 2015.
- [30] H. L. Fierstine and V. Walters, "Studies in locomotion and anatomy of scombroid fishes," in *Memoirs of the Southern California Academy of Sciences*, vol. 6, 1968, pp. 1–31. [Online]. Available: <https://pdfs.semanticscholar.org/5ad3/dc2ad455b6bc4b307f6343231bc06d1e9745.pdf>



Xingyu Chen received the B.E. degree in electrical engineering and automation from the College of Nuclear Technology and Automation Engineering, Chengdu University of Technology, Chengdu, China, in 2015. He is currently pursuing the Ph.D. degree in control theory and control engineering with the Institute of Automation, Chinese Academy of Sciences, Beijing, China.

His current research interests include computer vision, deep learning, and underwater robotics.



Junzhi Yu (SM'14) received the B.E. degree in safety engineering and the M.E. degree in precision instruments and mechanism from the North University of China, Taiyuan, China, in 1998 and 2001, respectively, and the Ph.D. degree in control theory and control engineering from the Institute of Automation, Chinese Academy of Sciences (IACAS), Beijing, China, in 2003.

He is currently a Professor with the State Key Laboratory of Management and Control for Complex Systems, IACAS. His current research interests include biomimetic robots, intelligent control, and intelligent mechatronic systems.

Dr. Yu serves as an Associate Editor for the IEEE TRANSACTIONS ON ROBOTICS and IEEE/ASME TRANSACTIONS ON MECHATRONICS.



Zhengxing Wu received the B.E. degree in logistics engineering from the School of Control Science and Engineering, Shandong University, Jinan, China, in 2008 and the Ph.D. degree in control theory and control engineering from the Institute of Automation, Chinese Academy of Sciences (IACAS), Beijing, China, in 2015.

He is currently an Associate Professor with the State Key Laboratory of Management and Control for Complex Systems, IACAS. His current research interests include fast maneuvers of bio-inspired robotic fish and gliding motions of robotic dolphins.



Yan Meng received the B.E. degree in mechanical engineering from the School of Mechanical Engineering, University of Science and Technology Beijing, Beijing, China, in 2017. He is currently pursuing the Ph.D. degree in control theory and control engineering with the Institute of Automation, Chinese Academy of Sciences, Beijing.

His current research interests include robotic fish and robotic vision system.



Shihan Kong received the B.E. degree in automation from the School of Control Science and Engineering, Shandong University, Jinan, China, in 2016. He is currently pursuing the M.E. degree in control theory and control engineering from the Institute of Automation, Chinese Academy of Sciences, Beijing, China.

His current research interests include underwater robotics and underwater robotic vision.